Journal of Fluids and Structures (2001) **15,** 255–273
doi:10.1006/jfls.2000.0334, available online at http://www.idealibrary.com on IDEAL®

REDUCED-ORDER MODELS OF UNSTEADY VISCOUS FLOWS IN TURBOMACHINERY USING VISCOUS–INVISCID COUPLING

B. I. Epureanu

Department of Mechanical Engineering, McGill University
Montreal, QC, Canada H3A-2K6

K. C. Hall and E. H. Dowell

Department of Mechanical Engineering and Materials Science, Duke University
Durham, NC 27708, U.S.A.

(Received 23 March 1999, and in final form 3 July 2000)

The proper orthogonal decomposition technique is applied in the frequency domain to obtain a reduced-order model of the flow in a turbomachinery cascade. The flow is described by an inviscid–viscous interaction model where the inviscid part is described by the full potential equation and the viscous part is described by an integral boundary layer model. The fully nonlinear steady flow is computed and the unsteady flow is linearized about the steady solution. A frequency-domain model is constructed and validated, showing to provide similar results when compared with previous computational and experimental data presented in the literature. The full model is used to obtain a reduced-order model in the frequency domain. A cascade of airfoils forming a slightly modified Tenth Standard Configuration is investigated to show that the reduced-order model with only 25 degrees of freedom accurately predicts the unsteady response of the full system with approximately 10 000 degrees of freedom.

1. INTRODUCTION

MODELING, PREDICTING, AND CONTROLLING aerodynamic flows is a complex spatio-temporal dynamical problem with important practical applications that holds the interest of many researchers. The recent rapid increase in the performance of computers allows one to construct and determine time histories and frequency-domain responses of extremely large aerodynamics systems, with up to 10^4–10^5 degrees of freedom. However, the computation time required to solve such systems is large and becomes prohibitive when parametric analyses are required. Moreover, most control schemes are designed for relatively small systems, with 1–100 degrees of freedom. Therefore, the applicability of these detailed and precise models is significantly limited. The need for models with a much smaller number of degrees of freedom, also called reduced-order models (ROM), is apparent.

Generally a ROM is a simplified model that has a much smaller number of degrees of freedom than the original model, but nevertheless captures the dynamics of the original model with acceptable accuracy. The tradeoff between accuracy and complexity is determined by each particular application. In most preliminary design analyses, the required level of accuracy is relatively low and, therefore, the use of a ROM may be acceptable. Also, many control strategies have a relatively large robustness to model uncertainties and thus may successfully control the full system although they are designed and tested using the ROM.

0889–9746/01/020255 + 19 $35.00/0

The early attempts to construct ROMs for fluid dynamic analysis and design used physical insights to reduce the complexity of the model (Whitehead 1959; Greitzer 1976; Moore & Greitzer 1986). Although useful, these techniques are usually applicable to a rather limited range of parameter variations, such as small values of the reduced frequency, and small static and dynamic loads. To overcome this limitation, more recent analyses have used more systematically derived ROMs. Among these techniques are Padé approximants of the unsteady aerodynamic transfer functions (Ueda & Dowell 1984; Peterson & Crawley 1988; Dowell 1980), eigenmode summation techniques in either time or frequency domains (Dowell 1995; Hall 1994), and proper orthogonal decomposition (Romanowski 1996). Most of these previous investigations have been concerned with linearized systems, although some of the techniques developed, e.g. POD, have been applied to model both linear and nonlinear phenomena (Kirby & Sirovich 1990; Noor 1994; Stone & Cutler 1996). Fully nonlinear normal modes and reduced-order models have also been investigated for very low-dimensional systems (Shaw & Pierre 1993, 1994).

Reduced-order models for a wide variety of systems have been constructed, e.g. Burger's model of turbulence (Canuto *et al.* 1988; Chambers *et al.* 1988), the full potential equation (Hall *et al.* 1995), Euler equations, Navier–Stokes equations (Deane *et al.* 1988), Raleigh–Bénard convection (Holmes *et al.* 1996), turbulence and boundary-layer models (Liu *et al.* 1994; Sirovich 1987*a–c*). Reduced-order models have been developed in the time domain for a variety of systems, e.g. flows over isolated airfoils. The flow was described by the Navier–Stokes equations which were used in the time domain to obtain the eigenmodes of the dynamics of the flow (Mahajan *et al.* 1991). Recently, however, the frequency domain was more extensively analyzed for both unsteady analyses and ROM construction (Kim *et al.* 1997; Buffum *et al.* 1998; Kim 1998). The inviscid full potential equation and the eigenmode summation technique in the frequency domain were used to construct ROMs (Hall *et al.* 1995) for flows in a turbomachinery cascade. A coupled inviscid–viscous model using the full potential equation and a finite-difference boundary-layer model was also used together with an eigenmode summation technique to construct ROMs (Florea *et al.* 1998) of the flow in a compressor cascade.

Significant progress has been made in the recent years in computing unsteady flows in turbomachinery and around isolated airfoils (Hall & Crawley 1989; Hall & Clark, 1993; Cizmas 1995; Verdon *et al.* 1995; Florea 1996). Various codes have been written using the Navier–Stokes equations. Although accurate, these codes have proven to be computationally very expensive. To reduce the complexity of the problem, many researchers have used simplifying assumptions in their models. One of these assumptions is the small disturbance assumption based on the observation that in many cases the unsteadiness in the flow has a smaller magnitude than the steady component. As a consequence, linearized Euler (Ni & Sisto 1976; Hall & Crawley 1989) and linearized Navier–Stokes (Clark 1998) codes have been developed.

The required computation time has been decreased by orders of magnitude compared to the time-marching of the fully nonlinear Navier–Stokes equations. However, the computation time still remains significant. Although historically it preceded the linearized Euler and Navier–Stokes codes, the boundary-layer assumption introduced by Prandtl is another effective way to further reduce the computational effort. In the boundary-layer assumption, one uses the fact that in many cases of practical interest, the Reynolds number is very large and the effect of the viscosity is limited to a thin region around the solid boundaries and the wake. Therefore, one may decompose the flow into an inviscid outer flow and a viscous inner flow. To complete the model, one defines the coupling mechanism that governs the inviscid–viscous interaction. When this interaction is weak, the viscous and inviscid regions may be solved separately in an alternative iterative fashion. The viscous flow equations or

boundary-layer equations are solved with a prescribed pressure on the solid boundaries, and the inviscid flow is solved with a given displacement thickness. This technique is known as the direct-coupling method.

Although the direct-coupling method works well in the weakly coupled regions, it converges very slowly or fails to converge when the interaction is strong. Typical examples of such interaction are encountered at leading and trailing edges, near shock waves, and near the separation point where the Goldstein singularity is present (Goldstein 1948). To account for such problems, many coupling techniques have been developed. These techniques may be classified as inverse, semi-inverse, quasi-simultaneous and simultaneous. The inverse technique (Catherall & Mangler 1966) solves the boundary-layer equations using a given displacement thickness rather than a given pressure while the potential equations are solved using a given pressure at the solid boundaries. The semi-inverse technique (LeBalleur 1978) solves both the boundary layer and the potential flow using a prescribed displacement thickness. At each iteration, a new value is prescribed for the displacement thickness based on a relaxation formula that uses viscous and inviscid predictions for the pressure. The quasi-simultaneous technique (Veldman 1979, 1981) uses a prescribed pressure for both viscous and inviscid regions together with a coupling law called the interaction law. The interaction law allows the scheme to solve simultaneously the viscous and inviscid regions. However, after each solution is obtained, new iterations are required until the prescribed pressure is identical to the viscous and inviscid pressure values as obtained from the outer (inviscid) and inner (viscous) solutions. The fully simultaneous technique solves both the viscous and inviscid regions simultaneously using the tangential velocity at the displacement body and the transpiration velocity to account for the displacement thickness. As opposed to the quasi-simultaneous technique, no iterations are required in the fully simultaneous method once the simultaneous set of equations is solved.

To further lower the complexity of the model without significantly affecting its accuracy, reduced-order models may be constructed using various techniques. In this paper, we propose the use of the proper orthogonal decomposition (POD), also known as Karhunen–Loève method. The POD is a technique that allows one to obtain good approximations of the spatial modes of vibration and the dynamics of a system using the response of the system to various excitations. Introduced in the context of meteorology and wind engineering to analyze experimental data (Cenedese *et al.* 1997; Jeong & Bienkiewicz 1997; Kikuchi *et al.* 1997; Sahan *et al.* 1997; Tamura *et al.* 1997), the POD has been used for a wide variety of problems, such as wind loads calculations (Ho *et al.* 1995; Bienkiewicz 1996; Uematsu *et al.* 1997). The wide applicability of the method is due to the fact that it is only based on the assumption of a low-dimensionality of the dynamics of large systems (Chambers *et al.* 1988; Georgiou & Schwartz 1996). For a large category of problems, this assumption holds because in many cases the energy of the dynamics of the system being analyzed is, to a very large extent, contained in the dynamics of a few modes of vibration.

In the context of turbulent flows, the POD was adopted as a technique that allows for the identification of coherent structures that naturally form in the flow (Sirovich 1987*a–c*; Holmes *et al.* 1996). The coherent structures that contain most of the energy of the dynamics are usually the most important.

Very well-suited for linear systems, the POD is also applicable to nonlinear systems. However, for some nonlinear systems, the applicability of the POD method is quite limited, because modes or coherent structures strongly exchange energy and therefore the required number of modes that may capture most of the energy of the dynamics increases very rapidly. This phenomenon occurs because the dynamics of the system is not low-dimensional (Strain & Greenside 1998). Typical cases of systems where the simple POD technique is not successful are the systems that exhibit spatio-temporal chaos. However, in such

situations, the POD may also be used in a local fashion. When spatio-temporal chaos is present, usually there are unstable limit cycles embedded into the strange attractor on which the dynamics collapses. The dynamics along these limit cycles is low-dimensional, and therefore local reduced-order models may be constructed. Using the low-dimensional approximate dynamics along the limit cycles one may design controllers that will stabilize these limit cycles (Epureanu & Dowell 1997, 1998; Epureanu *et al.* 1998).

In this paper, reduced-order models in the frequency domain are constructed to model the unsteady flow in a turbomachinery cascade. The fully nonlinear steady flow is computed first. The unsteady flow equations are then linearized about the nonlinear steady response. A frequency-domain linearized model is constructed, and the proper orthogonal decomposition in the frequency domain is applied to obtain several reduced-order models. The flow is modeled using an inviscid–viscous interaction technique. The inviscid part is described by the full potential equation using a variational formulation (Bateman 1930; Hall 1993). The viscous part is described by an integral boundary-layer model (Cizmas 1995; Cizmas & Hall 1995; Drela 1986, 1996; Nishida & Drela 1995) based on a set of correlation functions derived from analytical, numerical and experimental data. This model is presented in the following section. In Section 3, numerical results obtained with this model are compared to previous calculations and experimental data. The proper orthogonal decomposition is presented in Section 4, and is used to construct reduced-order models. Finally, in Section 5, we show representative results obtained using the reduced-order models.

2. MODELING

The model presented in this paper uses the small disturbance assumption together with the thin boundary-layer approximation. Also, a simultaneous scheme that uses a variational formulation of the inviscid flow and integral equations for the viscous region is developed.

2.1. Inviscid Flow

For an irrotational flow, the velocity vector may be represented as the gradient of a scalar potential function. For the case of inviscid and non-heat-conducting flow, the general Navier–Stokes equations may be reduced to one single equation known as the full potential equation, which may be expressed as

$$\nabla^2\phi = \frac{1}{c^2}\left[\frac{\partial^2\phi}{\partial t^2} + 2\nabla\phi\cdot\frac{\partial\phi}{\partial t} + \frac{1}{2}\nabla\phi\cdot\nabla(\nabla\phi)^2\right], \tag{1}$$

where c is the local speed of sound given by

$$c = c_0 - (\gamma - 1)\left[\frac{\partial\phi}{\partial t} + \frac{1}{2}(\nabla\phi)^2\right], \tag{2}$$

with c_0 denoting the stagnation speed of sound.

To apply a standard finite-element technique, it is advantageous to recast equation (1) in integral form. The conservation of mass is embedded in a variational principle (Bateman 1930; Hall 1993) which states that for an unsteady, inviscid, irrotational flow that is temporally periodic with period T, the velocity potential that solves equation (1) in a simply-connected domain D is the potential that satisfies the boundary conditions and

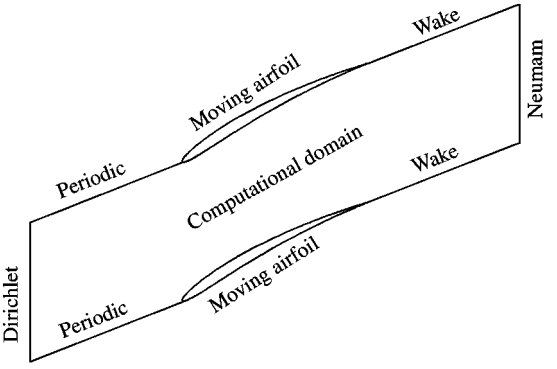

Figure 1. The solution domain and boundary conditions used to calculate the inviscid flow.

extremizes the functional Π given by

$$\Pi = \frac{1}{T}\int_T \iint_D p \, \mathrm{d}x \, \mathrm{d}y \, \mathrm{d}t + \frac{1}{T}\int_T \oint Q\phi \, \mathrm{d}\xi \, \mathrm{d}t, \tag{3}$$

where Q is the prescribed mass flux on the boundary and ξ is the distance along the boundary. As applied to flows in turbomachinery cascades, the simply-connected computational domain is obtained by making a cut along a line located close to the wake.

The steady flow is first solved. Then the unsteady flow is computed based on the small disturbance assumption. The potential is thus decomposed into a steady value Φ and an unsteady small magnitude potential φ periodically varying in time, such that

$$\phi(x, y, z, t) = \Phi(x, y, z) + \Re\left[\varphi(x, y, z)\mathrm{e}^{\mathrm{j}\omega t}\right] \tag{4}$$

with $\varphi \ll \Phi$, $\mathrm{j} = \sqrt{-1}$, and $\Re$ representing the real part.

Figure 1 shows the domain where the flow is solved and the regions where different boundary conditions apply. On the airfoil boundary, we require that the flux Q be equal to

$$Q = Q_{\text{airfoil}} = \rho \frac{\partial \phi}{\partial \mathbf{n}}, \tag{5}$$

where Q is a flux which arises from the motion of the airfoil and the thickening of the viscous boundary layer, and $\mathbf{n}$ is the local normal direction to the airfoil surface. The periodicity on the upstream region reads

$$\phi_{\text{up}} = \phi_{\text{down}}\mathrm{e}^{\mathrm{j}\sigma}, \tag{6}$$

where σ is the interblade phase angle. The wake boundary condition states that the jump in pressure across the wake is zero, i.e.,

$$p_{\text{up}} - p_{\text{down}} = 0. \tag{7}$$

Since the computational domain is not aligned with the wake, an additional unknown r is used to represent the displacement of the wake with respect to the boundary of the computational domain. To model a streamline along the wake, an additional injection flux is applied on the wake boundaries, i.e.,

$$Q_{\text{wake}} = \rho u \frac{\partial r}{\partial \xi}, \tag{8}$$

where u is the tangential velocity along the wake. For the steady problem, the upstream and downstream boundary conditions are Dirichlet and Newman, respectively. For the unsteady problem, the boundary conditions are exact nonreflecting boundary conditions (Hall *et al.* 1993) for the linearized unsteady problem.

2.2. Viscous Boundary Layer Flow

Starting from the Navier–Stokes equations, one may obtain the boundary-layer equations by performing a scale analysis under the assumption of a very large Reynolds number. One finds that the diffusion process parallel to a body surface and wake may be neglected, and that the momentum equation normal to the surface may be replaced by the condition of zero normal pressure gradient throughout the boundary layer. In this analysis, the local airfoil and wake curvature effects are neglected along with the local curvature deformation of the airfoil. Only the linearized local translation and rotation of the airfoil is analyzed.

The two unsteady compressible equations that describe the flow in the thin boundary layer are

$$\frac{\partial \rho}{\partial t} + \frac{\partial(\rho u)}{\partial \xi} + \frac{\partial(\rho v)}{\partial \eta} = 0, \tag{9}$$

$$\frac{\partial(\rho u)}{\partial t} + \frac{\partial(\rho u^2)}{\partial \xi} + \frac{\partial(\rho uv)}{\partial \eta} + \frac{\partial p}{\partial \xi} - \frac{\partial \tau}{\partial \eta} = 0, \tag{10}$$

where ξ and η are the tangential and normal directions to the surface of the body (Figure 2), and u and v are the tangential and normal components of the velocity, respectively. Equation (9) represents the conservation of mass, whereas equation (10) represents the momentum equation.

Formally integrating the conservation of mass and momentum equations, one obtains the von Kármán integral momentum equation

$$\frac{\partial}{\partial t}(\rho_e u_e(\delta^* - \delta_\rho)) + \frac{\partial}{\partial \xi}(\rho_e u_e^2 \theta) + \rho_e \delta_\rho \frac{\partial u_e}{\partial t} + \rho_e u_e \delta^* \frac{\partial u_e}{\partial \xi} - \frac{\rho_e u_e^2}{2} C_f + u_e Q_{\mathrm{BL}} = 0, \tag{11}$$

and the energy integral equation

$$\frac{\partial}{\partial t}(\rho_e u_e^2(\theta + \delta^* - \delta_\rho)) + \frac{\partial}{\partial \xi}(\rho_e u_e^3 \theta^*) + 2\rho_e u_e(\delta_\rho - \delta)\frac{\partial u_e}{\partial t} + 2\rho_e u_e^2 \delta^{**} \frac{\partial u_e}{\partial \xi} - 2\rho_e u_e^3 C_D + u_e^2 Q_{\mathrm{BL}} = 0, \tag{12}$$

where C_f is the wall shear stress coefficient, Q_{BL} is the wall transpiration due to the boundary-layer displacement thickness, and the subscript e indicates quantities measured at the boundary between the inviscid and viscous regions.

The formal integration leads to a number of unknown quantities such as the density thickness δ_ρ, the coefficient of dissipation C_D, the kinematic density displacement δ^{**}, etc. Based on both analytical solutions of simple flows and experimental data, researchers have developed correlation functions that describe the relationship between θ and δ^* and all the unknown quantities from equations (11) and (12) (LeBalleur 1978; Whitfield 1978; Veldman 1979; Whitfield *et al.* 1981; Drela 1986; Nishida & Drela 1995). The correlations used here include semi-empirical and empirical relationships between various integral boundary-layer characteristics, i.e.,

$$\delta = \int_0^\infty \left(1 - \frac{u}{u_e}\right) \mathrm{d}\eta, \qquad \theta = \int_0^\infty \left(1 - \frac{u}{u_e}\right) \frac{\rho u}{\rho_e u_e} \mathrm{d}\eta,$$

$$\delta^* = \int_0^\infty \left(1 - \frac{\rho u}{\rho_e u_e}\right) \mathrm{d}\eta, \qquad \theta^* = \int_0^\infty \left[1 - \left(\frac{u}{u_e}\right)^2\right] \frac{\rho u}{\rho_e u_e} \mathrm{d}\eta,$$

$$\delta^{**} = \int_0^\infty \left(1 - \frac{\rho}{\rho_e}\right) \frac{u}{u_e} \mathrm{d}\eta, \qquad \delta_\rho = \int_0^\infty \left(1 - \frac{\rho}{\rho_e}\right) \mathrm{d}\eta,$$

$$C_D = \frac{1}{\rho_e u_e^3} \int_0^\infty \tau_{\mathrm{wall}} \frac{\partial u}{\partial \eta} \mathrm{d}\eta, \qquad C_f = \frac{2}{\rho_e u_e^2} \tau_{\mathrm{wall}},$$

where τ_{wall} is the tangential wall shear stress.

Laminar-turbulent transition is of considerable practical interest because it controls important aerodynamic parameters such as drag and heat transfer. The Orr–Somerfeld equation, which governs the growth and decay of infinitesimal waves in the shear layer, was used here in combination with the e^n method to determine the location of the transition. The e^n method predicts the position of the transition to be the position where the overall maximum amplification of Tollmien–Schlichting disturbances is e^n and $n \approx 9$. We used the approximate spatial amplification curves derived by Drela (1986) based on the Orr–Somerfeld equation applied to a Falkner–Skan profile family.

This simple transition formulation was implemented using the similarity of the correlations defined by the laminar and turbulent coefficients of friction C_f and kinetic energy shape factors H^* at moderate Reynolds numbers typically found at transition. It has been found that the precise manner in which the transition occurs has little influence on the overall development of the boundary layer (Drela 1986). Consequently, we modeled the transition over only one discretization cell. We also used approximate value for C_f and H^* in the form of weighted averages of the laminar and turbulent values. For example, the transitional energy shape factor H^* is given by (Drela 1986)

$$H^*_{\mathrm{transitional}} = (1 - \gamma_{\mathrm{tr}}) H^*_{\mathrm{laminar}} + \gamma_{\mathrm{tr}} H^*_{\mathrm{turbulent}}, \tag{13}$$

where γ_{tr} describes the position of the transition inside a discretization cell

$$\gamma_{\mathrm{tr}} = \frac{(n_i - n_{\mathrm{critical}})}{(\mathrm{d}n/d\xi)|_i} \frac{1}{(\xi_i - \xi_{i-1})}, \tag{14}$$

i is the index of the transition cell, n_{critical} is a constant most often set to 9, and $\mathrm{d}n/\mathrm{d}\xi$ is empirically determined as a function of the shape factor H and $\mathrm{d}n/\mathrm{dRe}_\theta$.

We found that for the steady calculations, there is only a local small modification of the boundary layer when the linear interpolation is substituted with a simple unweighted average. However, an unweighted average induces discontinuities in the unsteady calculations due to the linearization. Therefore, we used equation (13).

The only parameter of the two boundary-layer equations in equations (11) and (12) that involves Reynolds stresses is the velocity-weighted integral in C_D. Due to the experimental evidence for upstream history effects on the Reynolds stresses, one introduces a lag equation that will correlate the dissipation factor to the shear stress coefficient given by

$$C_\tau = \frac{1}{u_e^2} \overline{u'v'}_{\max}, \tag{15}$$

where $\overline{u'v'}_{\max}$ is the maximum Reynolds stress (Drela 1986). The lag equation for the Reynolds shear stress scale was developed by Drela and Green (Green 1976; Green *et al.* 1977), starting from Bradshaw's (Cebeci & Bradshaw 1976) simplified model of the

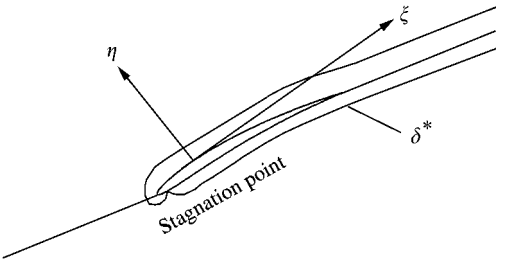

Figure 2. The solution domain used to calculate the viscous flow. A special local analytical solution is used at the stagnation point. The system of coordinates along the airfoil surface is indicated by ξ and η. A typical displacement thickness is sketched along the airfoil and wake.

turbulence kinetic energy transport equation, given by

$$\frac{\delta}{u_e^3 C_\tau U_{\max}} \frac{\partial}{\partial t}(u_e^2 C_\tau) + \frac{\delta}{u_e^2 C_\tau} \frac{\partial}{\partial \xi}(u_e^2 C_\tau) + K_c (C_\tau^{1/2} - C_{\tau eq}^{1/2}) = 0, \tag{16}$$

where $U_{\max}$ is the equilibrium slip velocity at the location of maximum shear stress, $C_{\tau eq}$ is the equilibrium shear stress coefficient, and $K_c = 5.6$ is an empirical constant (Drela 1996). We used equation (16) together with correlations for the equilibrium, self-preserving flow shear stress and edge velocity gradient.

The solution domain used to compute the viscous flow is shown in Figure 2, where the thickness of the domain is considered small in comparison to the airfoil-to-airfoil gap. The steady integral boundary-layer equations are parabolic in space so that boundary conditions have to be applied only at the stagnation point. Close to the stagnation point, the flow is similar to a flow over a wall. There is an analytical similarity solution for this flow that relates the displacement thickness to the inviscid tangential velocity (Cebeci & Bradshaw 1977). This similarity solution was used for the boundary condition at the stagnation point.

2.3. Viscous–Inviscid Coupling

The coupling between the inviscid and viscous regions is of major importance, especially at the trailing edge where the Kutta condition applies. The tangential inviscid velocity has a strong variation in this region. The strong variation has not only a local effect, but also a global effect on the characteristics of the flow. The inviscid–viscous coupling was implemented using an injection velocity (wall transpiration). This velocity is equal and of opposite sign to the entrainment velocity, and may be obtained starting from the continuity equation in defect form, i.e.,

$$\frac{\partial(\rho_{\text{inv}} - \rho)}{\partial t} + \frac{\partial(\rho_{\text{inv}} u_{\text{inv}} - \rho u)}{\partial \xi} + \frac{\partial(\rho_{\text{inv}} v_{\text{inv}} - \rho v)}{\partial \eta} = 0, \tag{17}$$

where the subscript inv indicates inviscid variables. Under the assumption of a first-order match at the boundary layer, one concludes that $\rho_e = \rho_{\text{inv}}$ and $u_e = u_{\text{inv}}$. Also, the component of the velocity normal to the surface is expanded in a Taylor series, retaining the first two terms in the series. Finally, imposing the matching condition at the body

surface, one obtains

$$Q_{\mathrm{BL}} = \frac{\partial(\rho_e \delta_\rho)}{\partial t} + \frac{\partial(\rho_e \delta^* u_e)}{\partial \xi}. \tag{18}$$

On the airfoil surface, the transpiration flux Q_{BL} is added to the flux Q in the surface integral in the variational principle equation (3). In the wake, the transpiration flux is added to the injection due to the motion of the wake.

In the next section, results obtained using the model described above are presented. The results are shown to be in good agreement with other computational and experimental results presented in the literature.

3. CODE VALIDATION

A slightly modified Tenth Standard Configuration was used to validate the steady and unsteady calculations. For this configuration, one cascade of NACA-5506 airfoils of chord c is considered. The solidity of the cascade of blades G/c is 1·0, where G is the gap between the airfoils. The stagger angle γ is 45°. The far-field upstream Mach number M is 0·5, the inflow angle Θ is 55°, and the Reynolds number based on chord and upstream velocity Re is 10^5.

Figure 3 shows the computed steady pressure obtained using the inviscid–viscous interaction code, where the pressure coefficient is defined by $C_{\mathrm{P}} = (p - p_\infty)/(\frac{1}{2}\rho v_\infty^2)$, where v_∞ is the total velocity upstream in the far field. These results are in good agreement compared to the results obtained with a Navier–Stokes solver (Clark 1998). The inviscid–viscous calculation match very closely the Navier–Stokes results on the suction side, while on the pressure side the two results generally agree, except for the region close to the transition. In contrast, the coefficient of pressure obtained using an inviscid full potential solver is quite different from the viscous calculation. The change in C_{P} due to the presence of viscosity is well captured by the inviscid–viscous code.

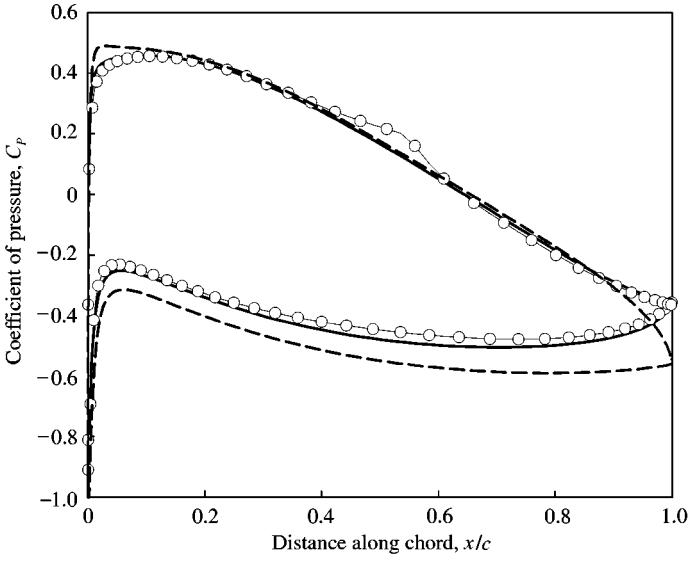

Figure 3. The coefficient of pressure obtained when the upstream far-field Mach number M is 0·5 and the Reynolds number is 10^5: —, Navier–Stokes; ○—○, inviscid–viscous; - - -, inviscid.

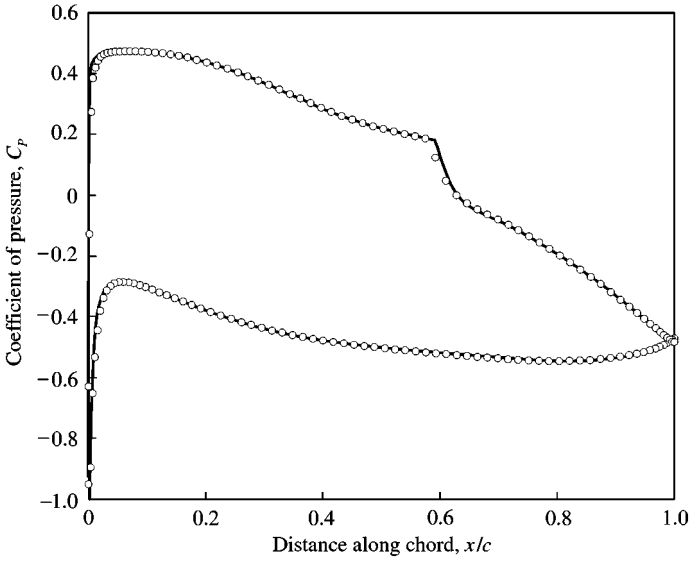

Figure 4. The coefficient of pressure obtained when an upstream far-field Mach number M is 0·5 and the Reynolds number is $0{\cdot}5 \times 10^6$: —, fine grid; ○, coarse grid.

Next, we investigate the sensitivity of the steady solution with respect to grid refinement. We compute the flow for a Reynolds number based on chord Re of $0{\cdot}5 \times 10^6$ using a fine and a coarse computational grid. The fine grid has 300×50 nodes while the coarse grid has 150×30 nodes. In Figure 4, a very good agreement between the results obtained with a fine and a coarse grid is observed.

Next, we investigate the sensitivity of the unsteady solution with respect to grid refinement. A pitching motion of the airfoils about their mid-chord point was considered. The interblade phase angle σ is 90°, the reduced frequency k is 0·85, and the Reynolds number based on chord Re is $0{\cdot}5 \times 10^6$. The reduced frequency k is defined as $k = \omega c/v_\infty$, where c is the chord and v_∞ is the total velocity upstream in the far field. Figure 5 shows a very good agreement between the unsteady coefficient of pressure obtained using a fine and a coarse grid. Also shown in Figure 5 is the unsteady coefficient of pressure obtained using an inviscid potential solver. Note that the results computed using the inviscid code are quite different from those obtained in the viscous computations. As expected, the differences are most significant in the region where the boundary layer is thick and separated.

The sensitivity of the unsteady solution with respect to grid refinement is observed for a broad range of reduced frequencies and interblade phase angles. Shown in Figures 6 and 7 are the computed unsteady lifts for a range of reduced frequencies and a full spectrum of interblade phase angles. The real part of the coefficient of lift C_L is presented for various interblade phase angles σ and reduced frequencies k. In Figure 6, the reduced frequency k is 0·85; in Figure 7, the interblade phase angle σ is 90°.

Next, we compare our method to experimental results for a cascade of blades as described by Buffum *et al.* (1998). The solidity of the cascade G/c is 0·657, and the stagger angle γ is 60°. The upstream far-field Mach number M is 0·2, the inflow angle Θ is 70°, and the Reynolds number based on chord Re is $0{\cdot}38 \times 10^6$. The airfoil pitches unsteadily about its mid-chord with amplitude 1·2°.

In Figure 8, the viscous–inviscid results are compared with the steady results obtained by Buffum *et al.* The coefficient of pressure obtained using the inviscid–viscous code is shown

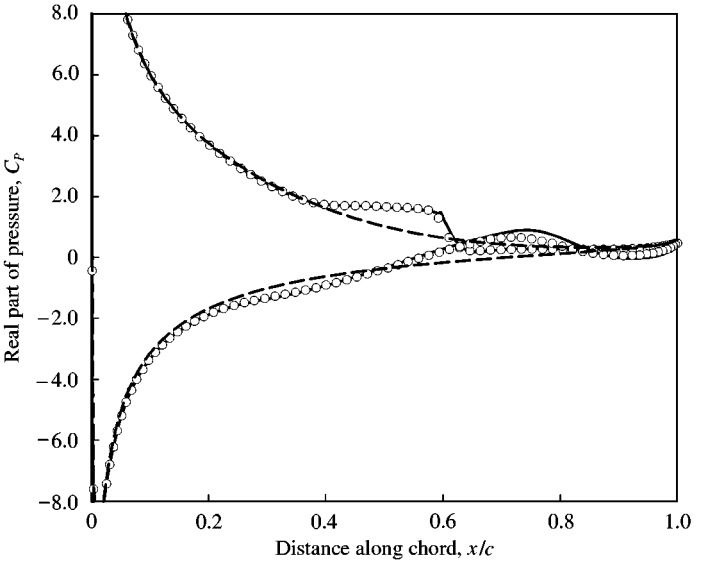

Figure 5. The real part of the unsteady coefficient of pressure C_P obtained when the interblade phase angle σ is 90°, the reduced frequency k is 0·85, and the upstream far field Mach number M is 0·5: —, fine grid; ○, coarse grid; - - -, inviscid.

to agree well with the experimental data when the transition from laminar to turbulent flow is established based on the experimental observations. The experimental observation of the transition point corresponds approximately to a value n_{critical} of 30. The inviscid–viscous code is shown to give, for this case, results as good as those from a Navier–Stokes solver (Clark 1998). However, the inviscid–viscous code gives different results when the transition is computed based on the empirical value n_{critical} of 10, a value determined from experimental observations of flows over isolated airfoils. The differences are mostly observed on the suction side where a large separation is present. The differences between the pressure results are due to the differences in determining the location of the laminar–turbulent transition, which strongly influences the region of separation. This calculation confirms that a good agreement is obtained when one uses additional experimental information in establishing the value of the transition parameter n_{critical}.

In Figures 9 and 10, the real and imaginary parts of the unsteady coefficient of pressure are presented. A fair agreement between the inviscid–viscous calculation and the experimental measurements and a Navier–Stokes solver is obtained. Similar to the steady case, the results obtained when n_{critical} is 30 are shown to agree better with the experiment than when n_{critical} is 10.

4. PROPER ORTHOGONAL DECOMPOSITION

First introduced in the time domain (Romanowski 1996), the POD has recently been used also in the frequency domain (Hall *et al.* 1999; Kim 1998). In this paper, we used the "snapshot" POD method. In this approach, the response of the linearized system with L degrees of freedom is obtained and stored in a solution vector $\mathbf{\Phi}_i$, for a set of N excitation frequencies ω_i. Each solution vector $\mathbf{\Phi}_i$ has L complex entries and, therefore, contains both the phase and the magnitude characteristics of the response. A matrix $\mathbf{R}$ of size $L \times N$ is formed such that its ith column is the solution vector $\mathbf{\Phi}_i$ for each $i \leqslant N$. A correlation

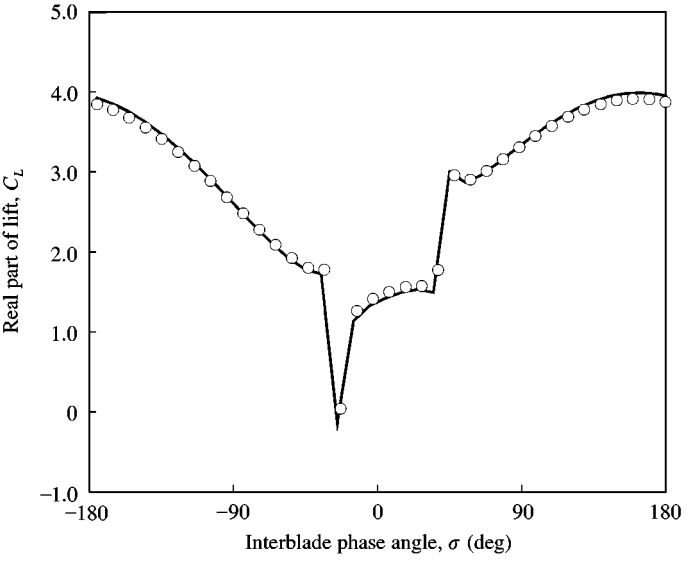

Figure 6. The real part of the coefficient of lift C_L obtained when the reduced frequency k is 0·85 and the upstream far-field Mach number M is 0·5: —, fine grid; ○, coarse grid.

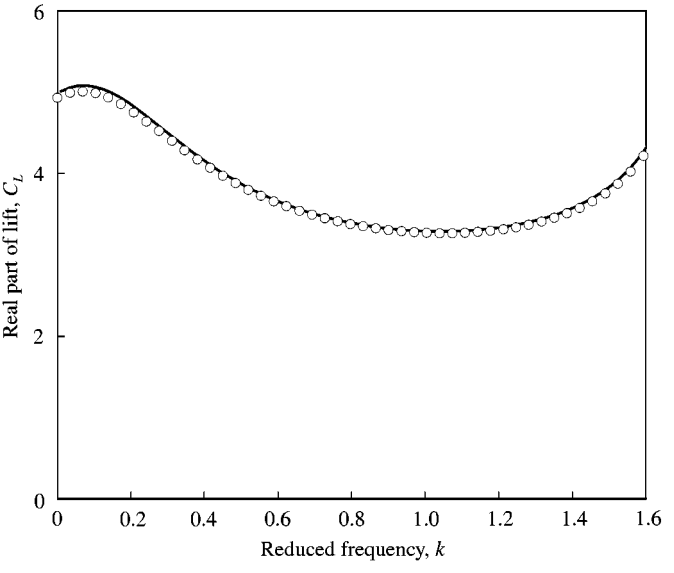

Figure 7. The real part of the coefficient of lift C_L obtained when the interblade phase angle σ is 90° and the upstream far-field Mach number M is 0·5: —, fine grid; ○, coarse grid.

matrix is then formed as

$$\mathbf{C} = \mathbf{R}^*\mathbf{R}, \tag{19}$$

where the superscript asterisk indicates the Hermitian operator. The POD eigenvalues are then obtained by solving an eigenvalue problem of dimension N,

$$\mathbf{C}\mathbf{v}_i = \lambda_i \mathbf{v}_i, \tag{20}$$

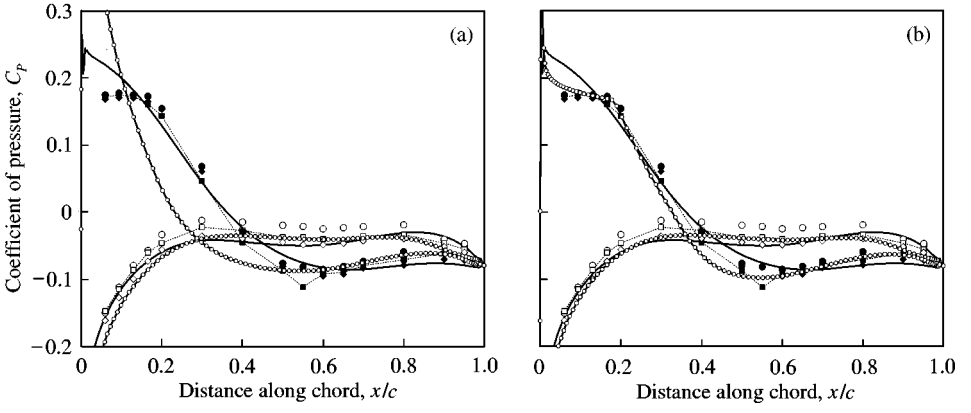

Figure 8. The steady coefficient of pressure C_P obtained experimentally and computed when n_{critical} is (a) 10 and (b) 30: —, Navier–Stokes; ●, experiment (suction); ○, experiment (pressure); ■—■, experiment (suction); □—□, experiment (pressure); ◆, experiment (suction); ◇, experiment (pressure); ○—○, inviscid–viscous.

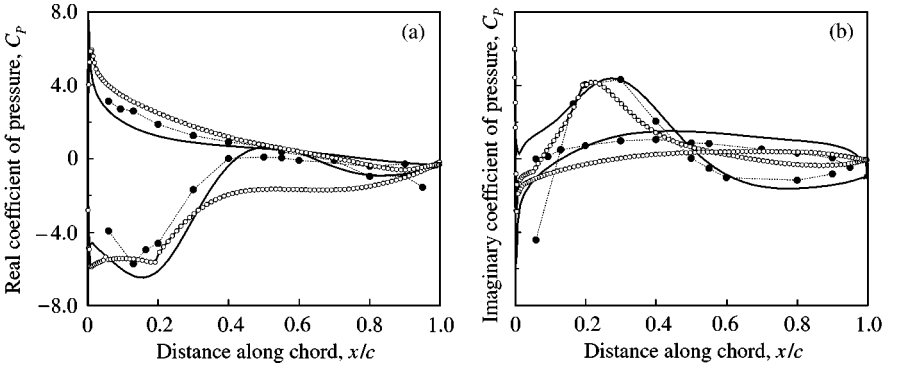

Figure 9. The real and imaginary parts of the unsteady coefficient of pressure C_P obtained experimentally and computed for $n_{\text{critical}} = 30$: —, Navier–Stokes; ●—●, experiment; ○—○, inviscid–viscous.

where i varies between 1 and N, λ is the reduced-order eigenvalue, and the $\mathbf{v}_i$ are eigenmodes of dimension N. Among the POD eigenvalues obtained, the most significant eigenmodes contain most of the energy of the dynamics and correspond to the largest eigenvalues. One organizes the reduced-order modes $\mathbf{v}_i$ and eigenvalues in descending order such that the first ones are the most significant.

The most significant n modes are then organized in a matrix $\mathbf{V}$ of size $N \times n$ such that the column i of $\mathbf{V}$ is vector $\mathbf{v}_i$, with $i = 1, \ldots, n$. The dynamical system is then projected onto the space spanned by these vectors and a reduced-order model is obtained. Formally, one may express the linearized equations of motion as

$$\omega^2 \mathbf{A}_2 \mathbf{\Phi} + \omega \mathbf{A}_1 \mathbf{\Phi} + \mathbf{A}_0 \mathbf{\Phi} = \mathbf{b}, \tag{21}$$

where $\mathbf{b}$ is the forcing vector. The component of the solution $\mathbf{\Phi}$ in the subspace S, is denoted $\mathbf{\Phi}_S$ and may be related to $\mathbf{\Phi}$ by

$$\mathbf{\Phi} = \mathbf{P}\mathbf{\Phi}_S. \tag{22}$$

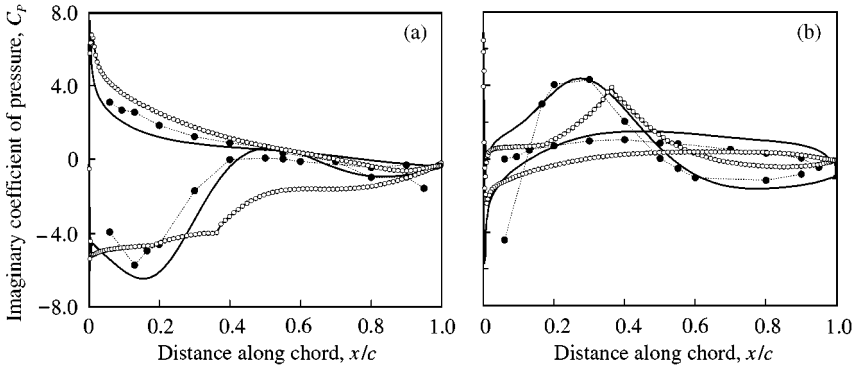

Figure 10. The real and imaginary parts of the unsteady coefficient of pressure C_P obtained experimentally and computed for $n_{\text{critical}} = 10$: —, Navier–Stokes; ●—●, experiment; ○—○, inviscid–viscous.

Multiplying equation (21) to the left by the Hermitian of the projection matrix $\mathbf{P} = \mathbf{RV}$, and considering only the solutions contained in the space $\mathbf{S}$ spanned by the columns of $\mathbf{P}$, one obtains a reduced-order system of size n as

$$\omega^2 \mathbf{P}^* \mathbf{A}_2 \mathbf{P} \mathbf{\Phi}_S + \omega \mathbf{P}^* \mathbf{A}_1 \mathbf{P} \mathbf{\Phi}_S + \mathbf{P}^* \mathbf{A}_0 \mathbf{P} \mathbf{\Phi}_S = \mathbf{P}^* \mathbf{b}, \tag{23}$$

Equation (23) represents the reduced-order model, and it is solved for the n unknowns $\mathbf{\Phi}_S$. These unknowns are then expanded back into the original physical space using equation (22). The most important feature of the POD technique is the fact that the eigenvalues of the reduced-order model in equation (23), are good approximations of the eigenvalues of the full system.

In the next section, a reduced-order model of a cascade of airfoils forming the Tenth Standard Configuration is investigated. The model is shown to provide accurate results over a wide range of reduced frequencies although only 25 modes are used. The original fluid model is therefore shown to be reducible from approximately 10 000 degrees of freedom to approximately 25 degrees of freedom.

5. REDUCED-ORDER MODELING

To show the applicability of the reduced-order technique, a typical cascade of NACA-5506 airfoils is analyzed. The solidity of the cascade G/c is 1·0, the stagger angle γ is 45°, the upstream far-field Mach number M is 0·5, and the inflow angle Θ is 55°. For the unsteady calculations, a pitching motion of the airfoils about the mid-chord point is assumed.

Three reduced-order models have been constructed. One model was obtained using a POD technique applied to a set of 75 snapshots obtained varying the interblade phase angle σ between -180 and 180° while the reduced frequency $k = \omega c/v_\infty$, was maintained constant of value 0·85. Another model was constructed using a POD technique applied to a set of 75 snapshots obtained varying the reduced frequency k between 0 and 1·75 while the interblade phase angle σ was maintained constant of value 180°. Finally, a third model was constructed using 10×10 snapshots obtained varying σ between $-180°$ and 180° and k between 0 and 1·75.

In Figure 11, the real part of the unsteady coefficient of pressure C_P obtained for an interblade phase angle σ of 90° and reduced frequency k of 0·85 is presented. A very good agreement is obtained between the full solution and the solutions obtained using the three reduced-order models. One reduced-order model was constructed using 25 POD modes

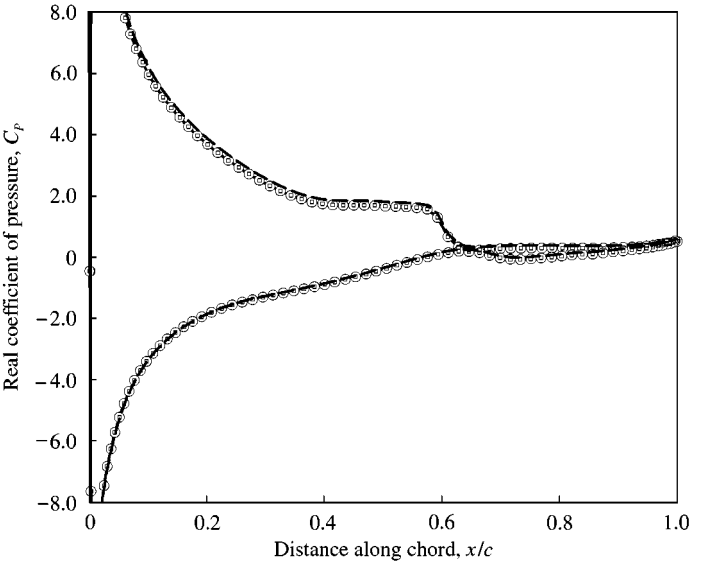

Figure 11. The real part of the coefficient of pressure C_P obtained using 25 POD modes when the interblade phase angle σ is 90°, the reduced frequency k is 0·85, and the upstream far-field Mach number M is 0·5: —, full model; ○, 25-mode model (σ); □, 25-mode model (k); - - -, 25-mode model (k and σ).

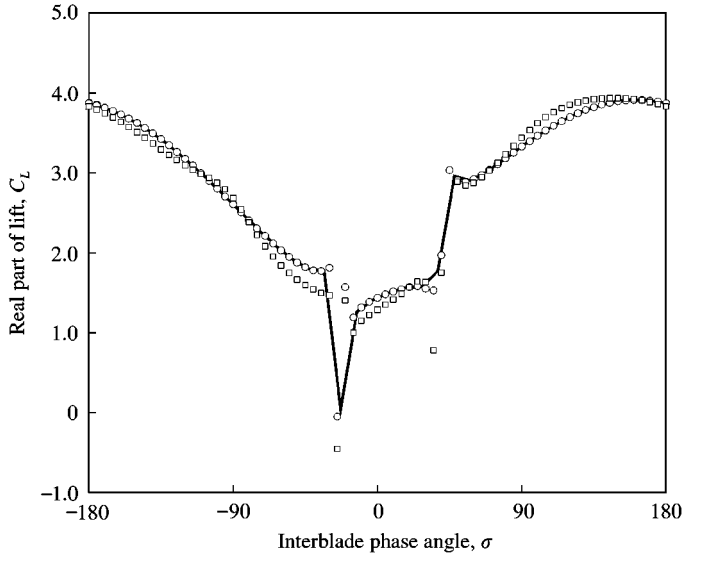

Figure 12. The real part of the coefficient of lift C_L obtained using 25 POD modes when the reduced frequency k is 0·85, and the upstream far-field Mach number M is 0·5: —, full model; ○, 25-mode model (σ); □, 25-mode model (k and σ).

based on snapshots obtained varying σ. Another model was built using 25 POD modes based on snapshots obtained varying k. Finally, the third model used 25 POD modes based on snapshots obtained varying both σ and k. The good agreement obtained shows that the dynamics of the flow is accurately captured by the first few POD modes.

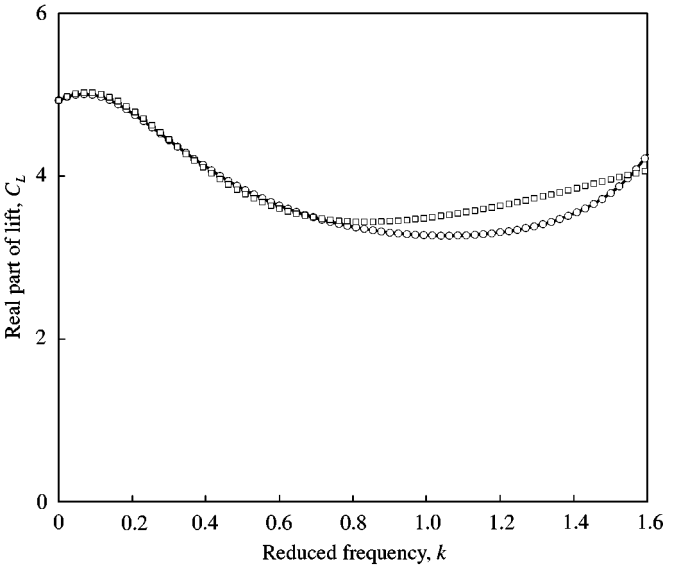

Figure 13. The real part of the coefficient of lift C_L obtained using 25 POD modes when the interblade phase angle σ is 90°, and the upstream far-field Mach number $M = 0{\cdot}5$: —, full model; ○, 25-mode model (k); □, 25-mode model (k and σ).

In Figure 12, the real part of the coefficient of lift C_L for a reduced frequency k of 0·85 and various interblade phase angles σ is presented. A good agreement is obtained between the full solution and two reduced-order models. One ROM was constructed using with 25 degrees of freedom obtained from POD snapshots computed varying σ. The other model was built using 25 POD modes obtained varying both σ and k. As expected, the reduced-order model obtained for fixed k gives more accurate results. Also, the most significant differences are obtained close to the resonant frequencies because in these regions the errors made in approximating the modes of vibration of the fluid are most strongly amplified.

In Figure 13, the real part of the coefficient of lift C_L for an interblade phase angle σ of 90° and various reduced frequencies k is presented. The results obtained using the full model are compared to the results obtained two reduced-order models. Both reduced-order models use 25 POD modes obtained with 75 snapshots. In one model, the modes have been obtained using snapshots computed varying k and maintaining σ constant. In the other model, σ was varied and k was maintained constant. The two reduced-order models considered give accurate results at low frequencies. The model obtained at constant σ gives good results at higher frequencies also. As expected, the model based on snapshots obtained varying both σ and k gives moderately good results at high frequencies. However, when required, the accuracy of the results may be improved by using a larger number of snapshots in frequency, and a larger interval of frequencies.

6. CONCLUSIONS

A fully nonlinear steady model of the flow in a turbomachinery cascade has been developed. The unsteady flow has then been linearized about the nonlinear steady response and a frequency domain model has been constructed.

The flow has been solved using an inviscid–viscous model, where the inviscid part is described by the full potential equation, while the viscous part is described by an integral

boundary-layer model. This model has been validated and shown to provide similar results when compared with previous computational and experimental data presented in the literature.

A reduced-order model in the frequency domain has been constructed using the proper orthogonal decomposition. A cascade of airfoils forming a slightly modified Tenth Standard Configuration has been investigated. The reduced-order model with only 25 degrees of freedom has been shown to accurately predict the unsteady response over a wide range of reduced frequencies when compared with a full model with approximately 10 000 degrees of freedom.

References

Bateman, H. 1930 Irrotational motion of a compressible fluid. *Proceedings of the National Academy of Science* **16,** 816–825.

Bienkiewicz, B. 1996 New tools in wind engineering. In *Proceedings of the* 1994 *East European Conference on Wind Engineering*, Vol. 65, pp. 297–300. Warsaw, Poland: Elsevier.

Buffum, D. H., Capece, V. R., King, A. J. & El-aini, Y. M. 1998 Oscillating cascade aerodynamics at large mean incidence. *Journal of Turbomachinery* **120,** 122–130.

Canuto, C., Hussaini, M. Y., Quarteroni, A. & Zang, T. A. 1988 *Spectral Methods in Fluid Dynamics.* New York: Springer-Verlag.

Catherall, D. & Mangler, K. W. 1966 The integration of the two dimensional laminar boundary layer equations past the point of vanishing skin friction. *Journal of Fluid Mechanics* **26,** 163–182.

Cebeci, T. & Bradshaw, P. 1977 *Momentum Transfer in Boundary Layers.* Washington: Hemisphere Publishing.

Cenedese, A., Miozzi, M. & Querzoli, G. 1997 Comparison between fourier and proper orthogonal decomposition of a velocity field within a convective vessel. In *Proceedings of the Eighth International Conference on Computational Methods and Experimental Measurements*, Vol. 1, pp. 319–329, Rhodes, Greece. Computational Mechanics Publications.

Chambers, D. H., Adrian, R. J., Moin, P., Stewart, D. S. & Sung, H. J. 1988 Karhunen–Loève expansion of Burgers' model of turbulence. *Physics of Fluids* **31,** 2573–2582.

Cizmas, P. G. A. 1995 A simultaneously coupled potential-boundary layer model of stall flutter in turbomachinery. Ph.D. thesis, Duke University.

Cizmas, P. G. A. & Hall, K. C. 1995 Computation of steady and unsteady viscous flows using a simultaneously coupled inviscid–viscous interaction technique. *Journal of Fluids and Structures* **9,** 639–657.

Clark, W. S. 1998 Investigation of unsteady viscous flows in turbomachinery using a linearized Navier–Stokes analysis. Ph.D. thesis, Duke University.

Deane, A. E., Kevrekidis, I. G., Karniadakis, G. E. & Orszag, S. A. 1988 Low-dimensional models for complex geometry flows: application to grooved channels and circular cylinders. *Physics of Fluids* **3,** 2337–2354.

Dowell, E. H. 1980 A simple method for converting frequency domain aerodynamics to the time domain. NASA Lewis Research Center.

Dowell, E. H. 1995 Eigenmode analysis in unsteady aerodynamics: Reduced order models. In *Proceedings of the* 36*th AIAA/ASME/ASCE/AHS/ASC Structures, Structural Dynamics, and Materials Conference*, Vol. 1, pp. 1–13, New Orleans, LA. Washington: AIAA.

Drela, M. 1986 Two-dimensional transonic aerodynamic design and analysis using the Euler equations. Ph.D. thesis, M.I.T.

Drela, M. 1996 Unsteady integral boundary layer equations with lag dissipation closure. Personal communication.

Epureanu, B. I. & Dowell, E. H. 1997 System identification for Ott–Grebogi–Yorke controller design. *Physical Review E* **56,** 5327–5331.

Epureanu, B. I. & Dowell, E. H. 1998 On the optimality of the OGY control scheme. *Physica D* **116,** 1–7.

Epureanu, B. I., Trickey, S. T. & Dowell, E. H. 1998 Stabilization of unstable limit cycles in systems with limited controllability: expanding the basin of convergence of OGY-type controllers. *Nonlinear Dynamics* **15,** 191–205.

Florea, R. 1996 Reduced order modelling and eigenvalue analysis of unsteady flows about oscillating airfoils and turbmachinery cascades. Ph.D. thesis, Duke University.

Florea, R., Hall, K. C. & Cizmas, P. G. A. 1998 Reduced-order modeling of unsteady viscous flow in a compressor cascade. *AIAA Journal* **36,** 1039–1048.

Georgiou, I. T. & Schwartz, I. B. 1996 Proper orthogonal decomposition approach to coupled structural–mechanics systems. In *Nonlinear Dynamics and Controls*, Vol. DE91, pp. 7–12. New York: ASME.

Goldstein, S. 1948 On laminar boundary layer flow near a position of separation. *Quarterly Journal of Mechanics and Applied Mathematics* **1,** 43–69.

Green, J. E. 1976 Application of head's entrainment method to the prediction of turbulent boundary layers and wakes in compressible flows. Aeronautical Research Council (U.K.) R.&M. 3788.

Green, J. E., Weeks, D. J. & Brooman, J. W. F. 1976 Prediction of turbulent boundary layers and wakes in compressible flows by a lag entrainment method. Aeronautical Research Council (U.K.), R.&M. 3791.

Greitzer, E. M. 1976 Surge and rotating stall in axial flow compressors. Part i: theoretical compression system model. *ASME Journal of Engineering for Power* **98,** 190–198.

Hall, K. C. 1993 Deforming grid variational principle for unsteady small disturbances flows in cascades. *AIAA Journal* **31,** 891–900.

Hall, K. C. 1994 Eigenanalysis of unsteady flows about airfoils, cascades, and wings. *AIAA Journal* **32,** 2426–2432.

Hall, K. C. & Clark, W. S. 1993 Linearized Euler predictions of unsteady aerodynamic loads in cascades. *AIAA Journal* **31,** 540–550.

Hall, K. C. & Crawley, E. F. 1989 Calculation of unsteady flows in turbomachinery using linearized Euler equations. *AIAA Journal* **27,** 777–787.

Hall, K. C., Florea, R. & Lanzkron, P. J. 1995 A reduced order model of unsteady flows in turbomachinery. *Journal of Turbomachinery* **117,** 375–383.

Hall, K. C., Lorence, C. B. & Clark, W. S. 1993 Nonreflecting boundary conditions for linearized unsteady aerodynamic calculations. In *Proceedings* 31*st Aerospace Sciences Meeting and Exhibit*, Vol. 93-0882, pp. 1–15, Washington: AIAA.

Hall, K. C., Thomas, J. P. & Dowell, E. H. 1999 Reduced-order modelling of unsteady small-disturbance flows using a frequency-domain proper orthogonal decomposition technique. In *Proceedings* 37*th Aerospace Sciences Meeting and Exhibit*, Reno, NV. AIAA paper 99-0655.

Ho, T. C. E., Davenport, A. G. & Surry, D. 1995 Characteristic pressure distribution shapes and load repetitions for the wind loading of low building roof panels. *Journal of Wind Engineering and Industrial Aerodynamics* **57,** 261–279.

Holmes, P., Lumley, J. L. & Berkooz, G. 1996 *Turbulence, Coherent Structures, Dynamical Systems and Symmetry*. Cambridge: Cambridge University Press.

Jeong, S. H. & Bienkiewicz, B. 1997 Application of autoregressive modeling in proper orthogonal decomposition of building wind pressure. *Journal of Wind Engineering and Industrial Aerodynamics* **71,** 685–695.

Kikuchi, H., Tamura, Y., Ueda, H. & Hibi, K. 1997 Dynamic wind pressures acting on a tall building model—proper orthogonal decomposition. *Journal of Wind Engineering and Industrial Aerodynamics* **71,** 631–646.

Kim, T. 1998 Frequency domain Karhunen–Loéve method and its application to linear dynamic systems. *AIAA Journal* **36,** 2117–2123.

Kim, T., Nam, C. & Kim, Y. 1997 Reduced-order aeroservoelastic model with an unsteady aerodynamic eigenformulation. *AIAA Journal* **35,** 1087–1088.

Kirby, M. & Sirovich, L. 1990 Application of the Karhunen-Loève procedure for the characterization of human faces. *IEEE Transactions on Pattern Analysis and Machine Intelligence* **12,** 103–108.

Leballeur, J. C. 1978 Couplage visqueux-non visqueux: methode numérique et applications aux écoulements bidimensionnels transsoniques et supersoniques. *Recherche Aerospatiele* **2,** 65–76.

Liu, Z. C., Adrian, R. J. & Hanratty, P. 1994 Reynolds number similarity of orthogonal decomposition of the outer layer of turbulent wall flow. *Physics of Fluids* **6,** 2815–2819.

Mahajan, A. J., Dowell, E. H. & Bliss, D. B. 1991 Eigenvalue calculation procedure for Euler/Navier–Stokes solvers with application to flows over airfoils. *Journal of Computation Physics* **97,** 398–413.

Moore, F. K. & Greitzer, E. M. 1986 A theory of post-stall transients in axial compression systems: Parts I and II. *Journal of Engineering for Gas Turbines and Power* **108,** 68–76.

NI, R. H. & SISTO, F. 1976 Numerical computation of nonstationary aerodynamics of flat plate cascades in compressible flow. *Journal of Engineering for Power* **98,** 165–170.

NISHIDA, B. & DRELA, M. 1995 Fully simultaneous coupling for three dimensional viscous–inviscid flows. *AIAA*, Paper 95-1806-CP.

NOOR, A. K. 1994 Recent advances and applications of reduction methods. *Applied Mechanics Reviews* **47,** 125–145.

PETERSON, L. D. & CRAWLEY, E. F. 1988 Improved exponential time series approximation of unsteady aerodynamic operators. *Journal of Aircraft* **25,** 121–127.

ROMANOWSKI, M. C. 1996 Reduced order unsteady aerodynamic and aeroelastic models using Karhunen–Loève eigenmodes. In *Proceedings of the Sixth AIAA Symposium on Multidisciplinary Analysis and Optimization*, Bellevue, WA. AIAA Paper 96-3981.

SAHAN, R. A., KOC-SAHAN, N., ALBIN, D. C. & LIAKOPOULOS, A. 1997 Artificial neural network-based modeling and intelligent control of transitional flows. In *Proceedings of the* 1997 *IEEE International Conference on Control Applications*, Vol. 1, pp. 359–364. Hartford, CT: IEEE.

SHAW, S. W. & PIERRE, C. 1993 Normal modes for non-linear vibratory systems. *Journal of Sound and Vibration* **164,** 85–124.

SHAW, S. W. & PIERRE, C. 1994 Normal modes of vibration for non-linear continuous systems. *Journal of Sound and Vibration* **169,** 319–347.

SIROVICH, L. 1987*a* Turbulence and the dynamics of coherent structures. Part I: coherent structures. *Quarterly of Applied Mathematics* **XLV,** 561–571.

SIROVICH, L. 1987*b* Turbulence and the dynamics of coherent structures. Part II: symmetries and transformations. *Quarterly of Applied Mathematics* **XLV,** 573–582.

SIROVICH, L. 1987*c* Turbulence and the dynamics of coherent structures. Part III: dynamics and scaling. *Quarterly of Applied Mathematics* **XLV,** 583–590.

STONE, E. & CUTLER, A. 1996 Introduction to archetypal analysis of spatio-temporal dynamics. *Physica D* **96,** 110–131.

STRAIN, M. C. & GREENSIDE, H. S. 1998 Size-dependent transition to high-dimensional chaotic dynamics in a two-dimensional excitable medium. *Physical Review Letters* **80,** 2306–2309.

TAMURA, Y., UEDA, H., KIKUCHI, H., HIBI, K., SUGANUMA, S. & BIENKIEWICZ, B. 1997 Proper orthogonal decomposition study of approach wind—building pressure correlation. *Journal of Wind Engineering and Industrial Aerodynamics* **72,** 421–431.

UEDA, T. & DOWELL, E. H. 1984 Flutter analysis using nonlinear aerodynamic forces. *Journal of Aircraft* **21,** 101–109.

UEMATSU, Y., YAMADA, M., INOUE, A. & HONGO, T. 1997 Wind loads and wind-induced dynamic behavior of a single-layer latticed dome. *Journal of Wind Engineering and Industrial Aerodynamics* **66,** 227–248.

VELDMAN, A. E. P. 1979 A numerical method for the calculation of laminar, incompressible boundary layers with strong viscous–inviscid interaction. NLR, National Aerospace Laboratory, The Netherlands.

VELDMAN, A. E. P. 1981 New quasi-simultaneous method to calculate interacting boundary layers. *AIAA Journal* **19,** 79–85.

VERDON, J. M., BARNETT, M. & AYER, T. C. 1995 Unsteady aerodynamic models for turbomachinery aeroelestic and aeroacoustic applications. NASA Lewis Research Center.

WHITEHEAD, D. S. 1959 The vibration of cascade blades treated by actuator disk methods. *Proceedings of the Institution of Mechanical Engineers* **173,** 555–563.

WHITFIELD, D. L. 1978 Integral solution of compressible turbulent boundary layers using improved velocity profiles. Propulsion Wind Tunnel Facility, Arnold Air Force Station.

WHITFIELD, D. L., SWAFFORD, T. W. & JACOCKS, J. L. 1981 Calculation of turbulent boundary layers with separation and viscous–inviscid interaction. *AIAA Journal* **19,** 1315–1322.